ERICA

Engineered Calcium-Silicate-Hydrates for Applications

H2020-MSCA-ITN-2017 Grant Agreement no. 764691

Deliverable D7.4 / D28

NMR good practice guide

Deliverable No.	**D7.4 / D28**
Deliverable Title	**NMR good practice guide**
Deliverable Lead	**USurrey**
Dissemination Level	**Public**
Due Date	**31 Oct 2021 (extension requested to 28 Feb 2022)**
Submission Date	**07 Jan 2022**
Author	**Peter McDonald (USurrey)**
Contributors	**ESR 5 Örs Istok & ESR 9 Magdalena Janota (USurrey), ESR 4 Anastasiia Nagmutdinova (UNIBO), Agata Gajewicz-Jaromin (USurrey), Chris Cirel (MR Solutions Ltd)**

ERICA is funded by the European Union under the Horizon 2020
Marie Skłodowska-Curie – Innovative Training Network (ITN) programme

Experiences of implementing spatially resolved magnetic resonance for the characterisation of water sorption transport in cement based materials gained from the ERICA project: a guide to good practice

Peter J. McDonald[a,*], Agata M. Gajewicz-Jaromin[a], Ors Istok[a], Magdalena Janota[a], Anastasiia Nagmutdinova[b], Chris Cirel[c]

[a]*Department of Physics, University of Surrey, Guildford, Surrey, GU2 7XH, UK*
[b]*DICAM, University of Bologna, 40131 Bologna, Italy*
[c]*MR Solutions Ltd, Abingdon, OX14 1RL, UK*

1. Introduction

The ERICA project[1] called for the use of spatially resolved ^{1}H nuclear magnetic resonance (NMR), that is magnetic resonance imaging (MRI), for the characterisation of water sorption in cement based materials, most notably cement paste.

Our group had previously and extensively used bulk ^{1}H NMR relaxometry for the characterisation of water filled porosity in cement and published a *Good Practice Guide* in collaboration with the UK National Physical Laboratory (NPL)[1]. In this method, the distribution of ^{1}H NMR signal intensities with different nuclear spin relaxation times T_1 or T_2 are measured using saturation-recovery or Carr-Purcell-Meiboom-Gill (CPMG) experiments respectively and correlated with the amount of water in cement pores of different size. Either relaxation-time distribution can be measured without sample drying and hence their measurement makes for non-destructive and non-invasive methods of following the evolution of the (water filled) pore size distribution in cement with a time resolution of just a few minutes. In addition, using a so-called solid-echo experiment the ratio of chemically-bound to evaporable water can also be measured thereby providing full quantification of the water in the sample.

While we [2, 3], and others [4, 5, 6, 7, 8, 9], had used MRI to map water in cement based materials, the new work demanded greater assurance of the relaxation time quantification of porosity types than had, for the most part, hitherto been the case. This posed some challenges since MRI is normally best suited to the imaging of materials with T_2 relaxation times longer than those encountered in cement materials.

This report reviews what was achieved in ERICA with emphasis on the practical implementation of experiments rather than the cement-materials-science outputs of the work. Its purpose is to serve as a guide to those following who may wish to perform similar experiments. It is assumed that the reader is familiar with ^{1}H NMR relaxometry. If not, then it is advised to read the NPL Good Practice Guide first, [1].

2. Basic concepts in MRI

The most fundamental equation of NMR is the Larmor equation

$$f_0 = \frac{\gamma}{2\pi} B_0 \tag{1}$$

that describes the proportionality between the NMR resonance frequency, f_0 and the applied magnetic field strength, B_0. By convention, B_0 defines the z-axis of the experiment. The constant of proportionality is $\gamma/2\pi$ where γ is the magnetogyric ratio. For ^{1}H, $\gamma/2\pi$ is approximately 42.57 MHz/T.

In MRI, a magnetic field gradient is superimposed on the static field so as to spread the resonant frequencies of ^{1}H according to their spatial co-ordinate, r, where $r \in [x, y, z]$. The field gradient is normally created by switched electric current windings within the magnet and is defined by

$$g_r = \frac{\partial B_z}{\partial r} \tag{2}$$

so that

$$f_0(r) = \frac{\gamma}{2\pi}(B_0 + g_r r) \tag{3}$$

As a matter of course, the spectrometer demodulates the signal and displays it in baseband so that the measured

*p.mcdonald@surrey.ac.uk

[1]*Engineered Calcium-Silicate-Hydrates for Applications*, EC H2020-MSCA-ITN Grant Agreement No. 764692, https://cordis.europa.eu/project/id/764691 and https://www.erica-etn.eu

January 4, 2022

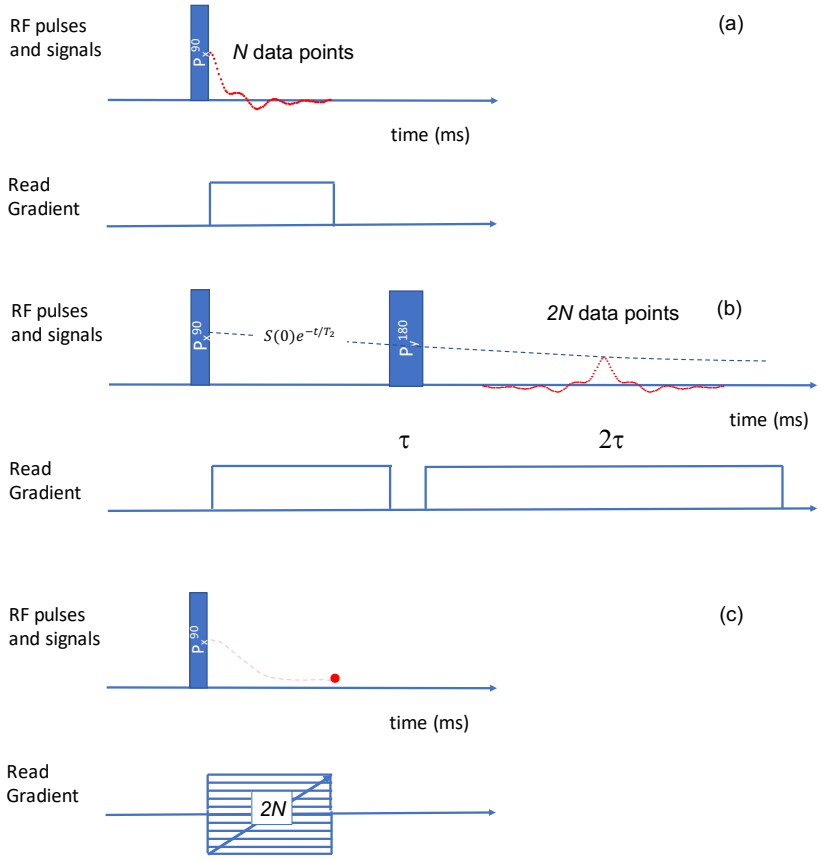

Figure 1: (a) A simple excitation pulse experiment carried out in the presence of a read gradient. The Fourier transform of the signal is a one dimensional profile of the ^{1}H density of the sample in the gradient direction (x, y or z). (b) The experiment is improved if the signal is recorded in the form of an echo. Issues of instantaneous gradient switching are avoided as the gradient is stabilised before data is acquired. The profile intensity is T_2 relaxation time weighted in so much as signal is only recovered from ^{1}H with $T_2 \gtrsim 2\tau$. (c) A phase encoded version of (a). The experiment is repeated for $2N$ values of the gradient varied from $-g_{max}$ to $+\frac{N-1}{N}g_{max}$. A single data point, red dot, is acquired each iteration. Each gradient "stretches" the decay signal in time by a different amount so that, by the end of the experiment, the same data as in (a) has been acquired (save for T_2 decay). The dash-line and red-dot data point illustrate the gradient increment $\sim g_{max}/4$.

signal frequency is

$$f(r) = f_0(r) - \frac{\gamma}{2\pi}B_0 = \frac{\gamma g_r r}{2\pi} \tag{4}$$

Fig. 1a shows a schematic of the simplest spatially resolved experiment possible. It implements a single 90° pulse excitation and free induction decay signal in the presence of a magnetic field gradient, conventionally known as a *read* gradient. For this experiment, the measured signal as a function of time is

$$S(t) = \int_{-\infty}^{+\infty} \rho(r) \exp(i\gamma g_r r t)\, \mathrm{d}r \tag{5}$$

where $i = \sqrt{-1}$ and $\rho(r)$ is the ^{1}H spin density at position r. The Fourier transform of the signal is a frequency spectrum. However, due to the one-to-one correspondence between frequency and position, so the spectrum has the appearance of a profile, or one-dimensional image of the sample.

The mathematical description is simplified by introducing the variable $k_r = \gamma g_r t/2\pi$. The variable k_r has units of inverse length and so is to r as f is to t. With this change of variable, we get

$$S(k_r) = \int_{-\infty}^{+\infty} \rho(r) \exp(i2\pi k_r r)\, \mathrm{d}r \tag{6}$$

It is obvious that $S(k_r)$ and $\rho(r)$ are a Fourier transform pair. Hence

$$\rho(r) = \int_{-\infty}^{+\infty} S(k_r) \exp(-i2\pi k_r r)\, \mathrm{d}k_r \tag{7}$$

but note that in Fig. 1a only positive k_r values are acquired.

In general, N discrete signal data points are recorded at intervals Δt such that $t_{max} = N\Delta t$. The Fourier transform is replaced by a discrete Fourier transform so that

$$\rho_p = \sum_{q=0}^{N-1} S_q \exp\left(-i\frac{2\pi pq}{N}\right) \tag{8}$$

where p and q are indices over spatial-profile and signal-data points respectively.

The profile spatial resolution (pixel size), Δr, and profile field of view, r_{FOV} are given by

$$\Delta r = \frac{r_{FOV}}{N} = \frac{2\pi}{\gamma g_r N \Delta t} = \frac{1}{k_r^{max}} \tag{9}$$

Since the encoding time cannot be substantially longer than T_2, (else the signal decays before it is measured) the best resolution that can be achieved for a given maximum available gradient strength is

$$\Delta r_{best} \approx \frac{2\pi}{\gamma g_r T_2} \tag{10}$$

Attempts to use a longer encoding time lead to a finer pixel size but not to improved resolution: the profile is blurred.

In practice, the experiment is rarely performed exactly as shown in Fig. 1a for a variety of reasons some of which are briefly considered below.

- A key advantage of MRI is the option to provide spatially resolved data with relaxation time contrast. To that end, signals are usually recorded in the form of spin-echoes using a $90_x\ \tau\ 180_y\ \tau\ echo$ pulse sequence. Fig. 1b shows the sequence and required gradient pulses. The magnetisation decays after the first pulse according to $\exp(-t/T_2)$. Therefore only ^{1}H with $T_2 \gtrsim 2\tau$ contribute substantially to the image. This is known as T_2 weighting.

- Nuclei require a time of the order of T_1 to recover following excitation before they are available for another "shot" of the experiment for the purposes of signal averaging or (see below) phase encoding. If the experimental recycle time is τ_{rd}, then only ^{1}H with $T_1 < \tau_{rd}$ contribute substantially to the image. Similar T_1 contrast can also be imposed by preceding, by a time τ_{sat}, the experiment with a saturation pulse in an experiment akin to a saturation-recovery T_1 measurement sequence. The signal is then weighted by $(1 - \exp(-\tau_{sat/rd}/T_1))$.

- By judicious choice of both $\tau_{echo} = 2\tau$ and $\tau_{sat/rd}$, it is possible to preferentially image just one population of ^{1}H in the sample, say water in large pores. This is because T_1 and T_2 normally increase with pore size in parallel. τ_{echo} selects for longer relaxation times (larger pores) and $\tau_{sat/rd}$ for shorter times (smaller pores). The pores that are visulaised are those having size in the range of selection overlap.

- Alternatively, multiple images may be acquired for a range of pulse timing parameters, in which case it is possible to fit the data, pixel-by-pixel, to the exponential spin relaxation equations and gain spatially resolved relaxation time distributions.

- Using an echo overcomes the practical difficulty of instantaneous switching on, and off, of the magnetic field gradient during a period of data acquisition. Gradient amplifiers have finite rise and fall times. Moreover, during switches the changing magnetic field induces electric eddy currents in the body of the magnet which induce spurious opposing gradient fields that take time to decay back down to zero. Therefore, during and immediately after a switch, the gradient strength is poorly defined. With an echo, the applied gradient field can be stabilised prior to data acquisition.

- Although there are some obvious and important practical differences, careful inspection of Eqn. 7 and the definition of $k_r = \gamma g_r t/2\pi$ shows that the mathematics cares little as to whether the signal is recorded (i) as a function of time during a continuously applied gradient pulse of constant strength or (ii) point-by-point at a constant time following gradient pulses stepped through a range of strengths. All that matters is that data is available for a range of k_r values. Recording data as a function of time (*i.e.* method i) is conventionally known as *frequency* encoding; as a function of gradient strength (*i.e.* method ii) as *phase* encoding. The phase encoded variant of Fig. 1a is shown in Fig. 1c. A key advantage of phase encoding is that, unlike frequency encoding, images are not distorted by magnet inhomogeneity and are much less prone to problems associated with gradient switching. The gradient pulses may not be "square" but the actual time-integrated gradient tends to increase linearly with requested pulse amplitude. The disadvantage of phase encoding is that the data points are recorded point-by-point and so the experiment takes much longer to perform.

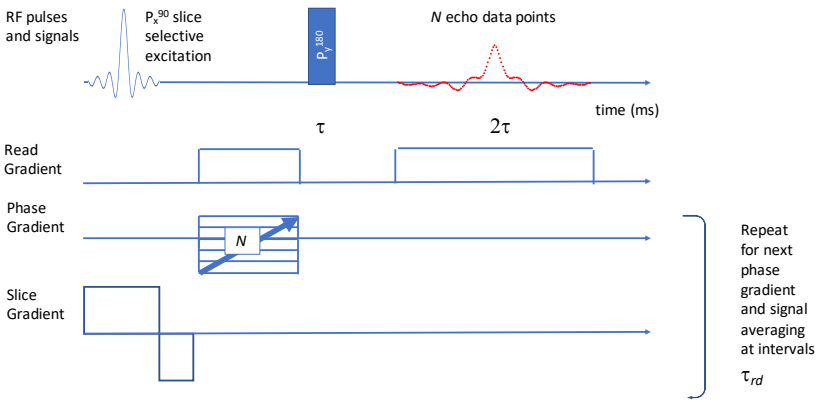

Figure 2: The 2DFT sequence which forms the basis of most standard MRI experiments. The top trace shows a slice selective excitation pulse and refocussing pulse leading to an echo signal at time 2τ. N data points are acquired. The next three traces show the read (frequency) and phase-encoding and slice selection gradients applied to any permutation of the x, y and z axes. The experiment is repeated for N values of the phase encode gradient. A 2D Fourier transformation of the N^2 data set yields the N^2 pixel image.The repetition time (τ_{rd}) and echo time (2τ) are chosen so as to preferentially map one or more ^{1}H population(s).

- As a final aside concerning echoes and phase encoding, notice that twice the number of data points are collected in Fig. 1b or c as compared to Fig. 1a and they span both positive and negative k_r. In the case of Fig. 1b, if the $2N$ points are collected at the same rate and in the same gradient strength, then the field of view is unchanged, but the pixel resolution is improved by a factor of 2. Alternatively, if the gradient strength is reduced by a factor of 2 and only N points collected, then the resolution stays the same but the signal-to-noise ratio is improved due to the lower data acquisition frequency bandwidth, $1/(2\Delta t)$. In other words, resolution and signal-to-noise ratio can be traded. A similar argument can be constructed for phase encoding.

- It has so far been assumed that the radio frequency excitation pulses are applied while the gradients are switched off. All ^{1}H in the sample are equally excited. However, it is possible to apply an excitation pulse in the presence of a gradient. The excitation pulse bandwidth, Δf is of the order of $1/t_p$ where t_p is the excitation pulse length. Hence, now, only ^{1}H in a narrow band, or slice, of the sample are excited. The slice thickness is given by

$$\Delta r_s = \frac{2\pi}{\gamma g t_p} \tag{11}$$

  Usually, the pulse is shaped in the time domain to give the slice sharp edges. Moreover, a refocussing gradient is additionally applied after the pulse to negate dephasing that occurred during the the pulse. Such pulses are known as slice selective pulses.

- In a highly optimised conventional imaging experiment, it is normal to select nuclei in a slice of the sample using slice selective excitation and then acquire a two dimensional spatially encoded data set for that slice using phase encoding in one direction, and frequency encoding in the other. The requisite pulse sequence is known as *2DFT* or *spin-warp*, [10]. One version is illustrated in Fig. 2.

3. MRI of cements: opportunity and requirement

Multi-dimensional ^{1}H MRI of cement based materials using 2DFT as just presented is, in principle, possible but very difficult. The short nuclear spin relaxation times in cements force the use of strong gradients or severely limit resolution. Strong gradients bring major problems associated with switching them on and off. Also, they increase the detection frequency bandwidth of the experiment so lowering greatly the signal-to-noise ratio. Hence, for given signal-to-noise, the experiments are made very slow. Poor resolution, typically measured in millimetres rather than microns, cannot compete with any of the alternate standard microscopies which greatly outperform MRI. Therefore MRI is not useful as a structural analysis tool for cement.

From the perspective of cement and concrete materials science, the strength of ^{1}H NMR is the ability to characterise water dynamics and water filled porosity in a sample with minimal, and certainly no destructive or

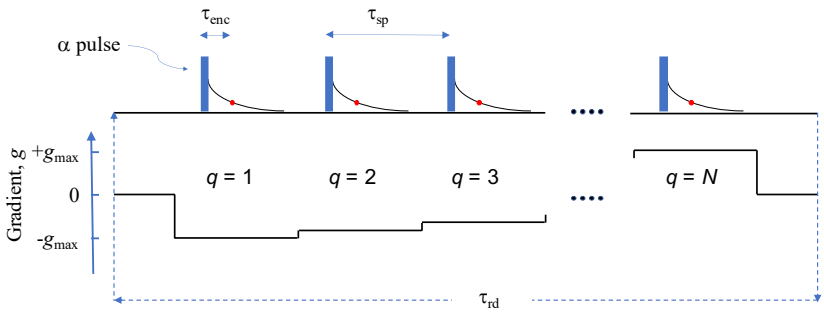

Figure 3: The SPRITE sequence consists of a chain of N low flip angle, α, excitation pulses with spacing τ_{sp} (upper trace) applied in a ramped magnetic field gradient, g (lower trace) that ranges from $-g_{max}$ to $+g_{max}$. A single data point is acquired a time τ_{enc} after each pulse. The N data points comprise a set which is Fourier transformed with respect to the product $k = \gamma g \tau_{enc}/2\pi$ to yield a spatial profile. The sequence is repeated with a repetition time τ_{rd} for purposes of signal averaging. Multiple data points with different τ_{enc} can be recorded in parallel to yield multiple data sets as discussed in the text.

invasive, sample preparation. To do this with spatial localisation is advantageous. One dimensional imaging (profiling) of water concentration profiles during transport into, or out of, a sample is a much more profitable use of the technology. Working in just one dimension leads to a substantial saving in experiment time. Moreover, profiling averages across a large orthogonal plane at each depth which, given that the aggregate size can be large, is advantageous. Indeed, it is sometimes even better to sacrifice imaging and instead to gather signal from just one small, but well defined, region *within* the bulk of the sample, *i.e.* to do spatially localised NMR, in order to have the most quantitative characterisation possible of spatially-localised pore-water-interactions in the shortest possible data acquisition time.

With this background, the choice of NMR / MRI pulse sequence for cement science is dictated by one primary consideration. We wish to acquire data rapidly along a profile-line or from a point in a sample with short T_2 relaxation times and to retain quantitative T_2 encoding. As already stated, the mainstream techniques are difficult. A somewhat different approach is required. Described below are three measurement protocols and measurement systems that we have found most suited to cement materials science within ERICA: SPRITE; GARField; and Unilateral Magnets.

4. SPRITE MRI

Balcom and co-workers [11, 12] have developed a suite of magnetic resonance imaging methods for short T_2 materials that collectively make use of SPI standing for single point imaging. The link between them is that they are all pure phase encode techniques (hence the name) which facilitates the use of strong magnetic field gradients while overcoming the requirement to switch those gradients rapidly through prohibitively large changes in strength. Of particular merit in the imaging of cement is SPRITE which stands for Single Point Ramped Imaging with T_1 Enhancement [13, 11]. SPRITE has been shown to be suitable for sorption studies in cores of cement based materials typically of a size measured in centimetres [9].

4.1. The SPRITE sequence and steady state free precession

The SPRITE sequence is shown in Fig. 3. It comprises a series of sub-90° excitation pulses (flip angle α) applied in relatively rapid succession with a spacing τ_{sp}. Data points are acquired at an encoding time τ_{enc} after each excitation pulse during the T_2^* decay of the nuclear magnetisation. A constant magnetic field gradient, g_q (the axis subscript r is dropped in favour of a counter-index q) is applied during the pulse and acquisition. The gradient strength is ramped between acquisitions in N equal steps between $-g_{max}$ and $+\frac{N-2}{N} g_{max}$. Data points are assembled into a phase-encoded data set $S(\tau_{enc}, \tau_{sp}, \alpha, g_{max})$ which is Fourier transformed with respect to $k = \gamma g \tau_{enc}/2\pi$ to reveal a profile of the sample.

Resolution of a SPRITE profile is given by

$$\Delta r = \frac{\pi}{\gamma g_{max} \tau_{enc}} \tag{12}$$

Notice that a factor of 2 is lost compared to Eqn. 9 because both positive and negative values of k-space (*i.e.* gradient) are sampled.

The field of view is $N\Delta r$.

The sub 90° excitation pulses have two advantages. The first is that they can be very short duration pulses. Short durations correspond to large frequency bandwidths. In a gradient field, the bandwidth corresponds to a distance ("slice-width") and this distance must be greater than the sample length, L. Eqn. 11 is modified to the requirement

$$L \ll \frac{2\pi}{\gamma g_{max} t_p} \tag{13}$$

Here, compared to Eqn. 11, the factor of 2 is not lost because it is the absolute strength of the (maximum) gradient that is of importance. The second advantage is to allow optimisation of the signal-to-noise ratio through a well established effect known as steady state free precession, [14].

Steady state free precession is to be understood as follows [15]. Consider a long chain of excitation pulses each of flip angle α and separation τ_{sp}. A data point is acquired after each pulse forming a data series $\{S_1, S_2, \cdots S_q, \cdots S_N\}$.

After a (surprisingly small) number of pulses, the magnetisation is in a state of dynamic equilibrium in so much as the magnetisation immediately preceding the q^{th} pulse must equal the magnetisation immediately preceding the $(q+1)^{th}$. In a constant magnetic field, the data acquisitions will be the same so that $S_q = S_{q+1}$.

Consider next that $\tau_{sp} \gg T_2$. Consider also that the equilibrium bulk magnetisation is M_0 along the z-axis and that the magnetisation preceding the q^{th} pulse is M^+, also along the z axis. The condition $\tau_{sp} \gg T_2$ ensures that by the time of the pulse, x and y components of the magnetisation have decayed to zero. The pulse tips a fraction $M^+ \sin(\alpha)$ of the magnetisation to the $x-y$ plane leaving $M^+ \cos(\alpha)$ along z. The z magnetisation starts to relax exponentially towards M_0 with a time constant T_1 according to

$$\frac{\mathrm{d}M_z}{\mathrm{d}t} = \frac{M_0 - M_z}{T_1} \tag{14}$$

Hence, M_z at time t following the pulse is given by $M_z(t) = M_0 - (M_0 - M^+ \cos(\alpha)) \exp(-t/T_1)$. The dynamic equilibrium requires that $M_z(\tau_{sp}) = M^+$ leading to

$$M^+ = M_0 \frac{1 - \exp(-\tau_{sp}/T_1)}{1 - \cos\alpha \exp(-\tau_{sp}/T_1)} \tag{15}$$

The signal intensity immediately following the pulse is $M^+_{xy} = M^+ \sin(\alpha)$. Fig. 4a shows a plot of M^+_{xy}/M_0 as a function of α for different values of τ_{sp}/T_1. For any finite τ_{sp}, M^+_{xy} is, of course, always less than M_0 and so

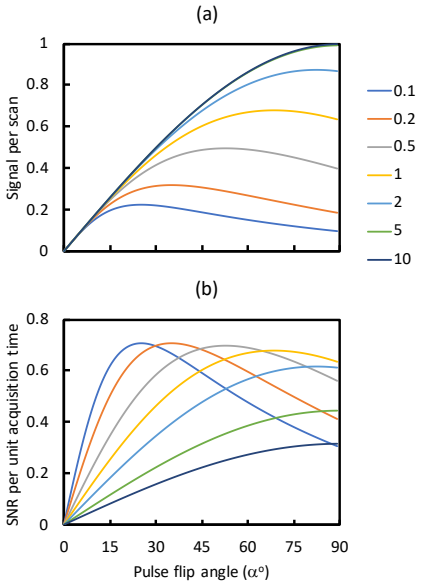

Figure 4: (a) The measured signal fraction (M^+_{xy}/M_0) as a function of pulse flip angle plotted for different values of the ratio τ_{sp}/T_1 ranging between 0.1 and 10. The maximum of each curve occurs at the Ernst angle. (b) The signal-to-noise ratio per unit total acquisition time. High signal-to-noise ratio can be achieved for low flip angle pulses applied in rapid succession.

sub optimal. However, it has a maximum at a flip angle less than 90° known as the Ernst angle. Moreover, the signal-to-noise ratio is proportional to $\sqrt{n}$ where n is the number of acquisitions. For a continuous chain of acquisitions, the number per unit time is τ_{sp}^{-1}. Therefore, the signal-to-noise ratio per unit acquisition time varies as $M^+_{xy}/\sqrt{\tau_{sp}}$. Fig. 4b shows how the signal-to-noise ratio varies for the same parameters as in Fig. 4a. It is immediately clear that significant improvements are to be gained through the use of rapidly applied, low flip angle pulses.

More extended analysis permits the restriction $\tau_{sp} > T_2$ to be lifted in which case an extended version of Eqn. 15 results. The analysis is to be found in the literature, [15]. It is critical to medical MRI where both T_1 and T_2 are long, but much less so in cements where it is easy to arrange $\tau_{sp} > T_2$.

4.2. Multiple experiments

Multiple experiments can be performed for different τ_{enc} in order to learn about the sample T_2 (pore size) distribution. However, this is very time consuming. To save time, multiple data points may be acquired for different encoding times after each pulse and split into different data sets in post-processing. In order to keep the

spatial resolution and field of view the same for each encoding time, τ_{enc}, more gradient steps are included than necessary for any one profile. For the shortest encoding time profile, data is sampled from every k^{th} gradient step up to the absolute gradient strength maximum whereas for the longest encoding time profile, data is sampled every step up to $1/k$ the absolute gradient strength maximum. Accordingly, $\tau_{enc}^{max} = k\tau_{enc}^{min}$. In similar fashion, intermediate encoding times sample data at appropriately scaled step intervals. Significant time is saved because most steps contribute to more than one profile - the middle one contributes to them all! These ideas are illustrated in Fig. 5.

4.3. Experimental experience

The equipment used at the University of Surrey comprised a 20 cm diameter bore, 60 MHz ^{1}H NMR superconducting magnet fitted with a Resonance Research Inc actively shielded gradient set with a 10 cm internal diameter access space powered by Techron 9900 series amplifiers. Within the gradient set is a 27 mm internal diameter cylindrical, birdcage NMR coil 80 mm in length that comfortably accommodated 60 mm long, 25 mm diameter cylindrical cement samples. Although a handful of 2 and 3D SPRITE experiments were performed, for the most part within ERICA, it was used for capillary sorption experiments where water sorption along the length of the sample was performed outside of the magnet. The lateral sides of the samples were sealed with tape. In the 1D sorption work, data for 19 encoding times τ_{enc} uniformly spaced from 100 to 1000 μs were acquired, although only data for $\tau_{enc} \geq 200$ μs was actually used in the analysis. With just two data points at most spanning the T_2 range of inter-layer water (≈ 100 μs), it was not possible to accurately quantify inter-layer water and its inclusion led to large errors. The pulse gap was $\tau_{sp} = 1500$ μs with $N = 128$ gradient steps. A total of 32 scans were recorded for signal averaging with a repetition time of $\tau_{rd} = 1.5$ s for each τ_{enc}. We did not regularly use multi τ_{enc} values each ramp (Sect. 4.2) for fear of overheating the gradients. The nominal pulse flip angle was $\alpha = 45°$. The maximum gradient strength was adjusted to give a profile field of view of 200 mm leading to a spatial resolution of ≈ 1.3 mm. The largest gradient is required for the shortest encoding time and was here about 0.09 T/m.

4.4. SPRITE data analysis

Basic data processing is very standard. A data set $S(\tau_{enc}, \tau_{sp}, \alpha, g_{max})$ is Fourier transformed to yield the spatial profile, $I(\tau_{enc}, \tau_{sp}, \alpha, z)$ where z is position using a discrete Fourier transform algorithm, *viz*:

$$I(z_p) = \sum_{q=0}^{N-1} S(g_q) \exp\left(-i\frac{2\pi pq}{N}\right) \tag{16}$$

where $i = \sqrt{-1}$ and $z_p = p\pi/\gamma g_{max}\tau_{enc}$.

In practice, within ERICA we included a number of additional steps.

- Data filtering

Data sets are sine-bell filtered before Fourier transformation to reduce high frequency noise in the spatial profile according to

$$S^{filt}(g_q) = S(g_q) \times \sin\left(\frac{q\pi}{N}\right) \tag{17}$$

- Non-uniform pulse flip-angle mitigation

Ideally, the low flip angle pulses are sufficiently short that their bandwidth fully spans the frequency bandwidth of the sample in the magnetic field gradient. In practice, the pulse bandwidth falls off towards the sample ends and for this reason the profile intensities post Fourier transformation were corrected by the intensity of a uniform standard sample. The α dependency of the profile intensity for given τ_{enc} is dependent on the relaxation time T_1. Therefore the uniform sample should have comparable T_1. Within ERICA we used a uniformly saturated, and well hydrated, cement paste measured prior to drying or (less frequently) after re-wetting. Unfortunately, this correction is not perfect when there is a distribution of T_1 so it is worth ensuring that Eqn. 13 is met as fully as possible.

- Long term instrumentation stability

Sorption measurements were sometimes made weeks apart. A rubber sample was measured and used to check for, and where necessary correct for, *e.g.* long term drift in instrumentation amplifier gain or changes to the probe Q factor approximately given by the NMR frequency divided by the excitation coil tuning bandwidth.

- Phase rotation of data

The modulus (magnitude mode) of the profile intensity was taken to guard against systematic, but uncontrolled, phase rotations across data sets. The downside of this procedure is that an apparent, but not "true", baseline offset is introduced into plots of $I(\tau_{enc})$ against τ_{enc}.

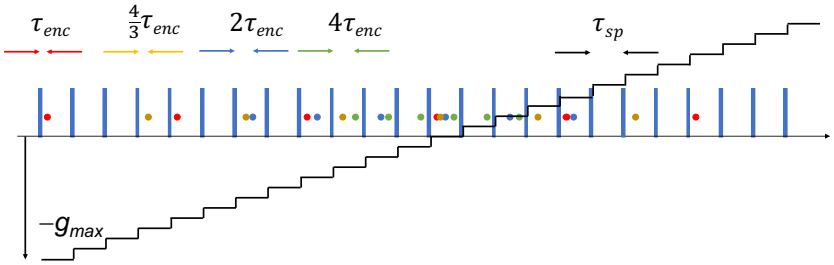

Figure 5: A schematic of a multiple profile SPRITE acquisition. 32 excitation pulses (blue rectangles) and a ramped gradient (black staircase trace) are shown. 8 data acquisition points are in red, each a time τ_{enc} after pulses separated by $4\tau_{sp}$. A further 8 are shown in each of: yellow $\frac{4}{3}\tau_{enc}$ after a pulse and separated by $3\tau_{sp}$; blue $2\tau_{enc}$ after a pulse and separated by $2\tau_{sp}$; and green $4\tau_{enc}$ after a pulse and separated by τ_{sp}. After Fourier transformation, each colour set yields a profile of the same field of view and resolution but with different encoding time so as to enable spatially resolved T_2 decay quantification.

- Spatially resolved porosity fraction analysis

Eqn. 15 gave M^+, the $z-$magnetisation available at each SPRITE excitation pulse. The measured signal intensity at time τ_{enc} after the pulse is therefore $M^+ \sin(\alpha) \exp(-\tau_{enc}/T_2)$. To find the local filled porosity fractions, data points at each location, z, for different encoding times, τ_{enc}, are fit to [13, 11] :

$$I(\tau_{enc}) = \sum_{i=1}^{\epsilon} I_0^i \frac{\exp\left(\frac{-\tau_{enc}}{T_2^i}\right)\left(1-\exp\left(\frac{-\tau_{sp}}{T_1^i}\right)\right)\sin\alpha}{1-\cos\alpha\exp\left(\frac{-\tau_{sp}}{T_1^i}\right)} \tag{18}$$

where ϵ is the presumed number of relaxation components and I_0^i are the different component amplitudes. To simplify the analysis, advantage is taken of the fact that $T_1^i = \beta T_2^i$ for pore water in cement, where β is a constant between 3 and 4. In ERICA we used $\beta = 4$.

It might be hoped to fit the decays to three components representing hydrate inter-layer, gel pore and inter-hydrate pore water. In practice within ERICA, for the sparse data available, we found this too difficult to do reliably. The fits were very sensitive to the first data point at acquisition time 100 μs. Therefore, we chose to exclude the first two data points so as to exclude almost all contribution from inter-layer water to the signal and instead fit to two components only assuming $T_2^{gel} = 250$ μs and $T_2^{cap} = 900$ μs.

Experimental results obtained using SPRITE applied to cement within ERICA are to be found in the literature, [16].

5. GARField

Whereas SPRITE is best suited to millimetre resolution in centimetre sized samples, GARField is best suited to sub-millimetre resolution in millimetre sized samples. GARField stands for Gradient at Right Angles to Field and refers to a specialist design of permanent magnet [17] with curved pole pieces and hence an inbuilt gradient field. It is purpose built for profiling through thin, planar samples with high spatial resolution, originally layers of paint. The small sample size allows small excitation coils and hence much shorter excitation pulse lengths and spectrometer dead-time. With short times it is possible once more to detect and quantify hydrate inter-layer water.

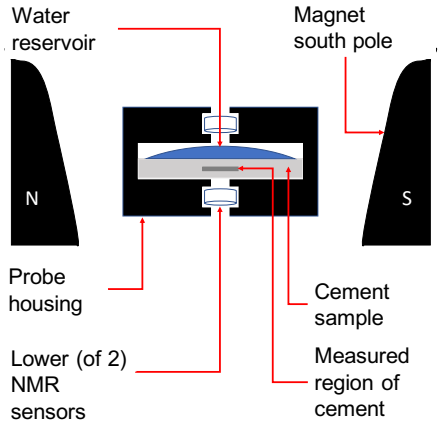

Figure 6: A schematic of the GARField magnet and probe as set up for a sorption experiment within the ERICA project. The magnet north and south pole pieces are shown to the left and right. Hence the B_0 field is horizontal. The shaped pole pieces create a strong field gradient in the orthogonal (vertical) direction. The probe casing (centre, in black) houses a cement disc (grey) and two NMR sensors (small coils of wire). The measured central slice of the cement disc is shown in darker grey. The cement disc is 15 mm diameter, 1.5 mm thick. The measured slice is $\sim$ 160 μm thick. Water (50-60 μL, blue) is placed on the upper surface of the sample through the top hole.

In ERICA, ^{1}H NMR measurements were made using a GARField design magnet operating at approximately 20 MHz. Fig. 6 shows a schematic of the setup. The GARField used incorporates a strong permanent magnetic field gradient of 9.16 T/m in the vertical direction so that the exact resonance frequency depends on depth into the sample with a rate of change of 390 Hz/μm. A probe was specially built to house and level a disc of cement paste 15 mm in diameter and up to 1.5 mm thick. The probe sealed around the circumferential edges of the sample. The probe was fitted with a Helmholtz-like pair of dual RF transmit / receive NMR coils of 5 mm diameter placed above and below the sample. This configuration ensured more uniform NMR signal excitation and detection through the depth of the sample. The small diameter of the coils ensured that signal was only detected from the central region of the circular disc, avoiding any potential circumferential edge effects. By varying the frequency, the depth of the region within the sample was chosen.

Four small holes in the probe, one above, one below and two to the side of the sample allowed the ingress and egress of either water or vapour. For wetting studies, a dried sample was placed in the magnet. A pre-wetting NMR measurement was made. The top hole was used to place a small volume (typically 50-60 μL) of water on the upper sample surface. NMR measurements were made throughout the wetting period, initially at about 4 minute intervals, more slowly as the experiment progressed to allow more averaging and better signal-to-noise ratio. Note, however, that multiple depths were examined, so data sets were not necessarily recorded at this rate at a single depth throughout. The lower hole was left open to allow air egress from below. The surface water was visible in the MRI and this facilitated periodic top-up of the water level. The pre-wetting MRI measurement was additionally used to locate the sample surface, to ensure that the sample was mounted level and to calibrate the measurement depth. For drying, an initially saturated sample was positioned in the magnet. A gentle air stream (60 L/hr) was passed through a large volume of dry silica gel and then onto the sample top surface though the top hole, exiting a side hole. Again periodic NMR measurements were made.

For the NMR, the quadrature echo train sequence was used. This is defined, in standard notation, by $P_x^{90} - \tau - \left(P_y^{90} - 2\tau -\right)_n$ where it is understood that the pulse length is set at the slice centre frequency and the frequency is set to the desired depth within the planar sample [18]. NMR echoes comprising $N = 16$ data points each acquired at a sampling rate $1/\Delta t = 1$ MHz were acquired during each of the $n = 64$ 2τ windows. The NMR frequency, f_0, was adjusted so that the resonance condition occurred at a depth of (normally) 600 μm in the sample. A value of $\tau = 20$ μs was used throughout so that the echo time spacing was $\tau_{echo} = 40$ μs. The repetition time was typically set at 0.1 s so that 2048 averages required about $3\frac{1}{2}$ min.

5.1. GARField Spatial Resolution

In GARField, the spatial resolution is controlled by two factors. First, the magnetic field gradient is necessarily on during the excitation pulse. As with SPRITE, the pulse has a bandwidth given approximately by $1/t_p$ and so excites magnetisation in a slice orthogonal to the gradient direction of thickness Δr_s as given by Eqn. 11. Second, the signal echo is acquired for a time $N\Delta t$ where N is the number of points acquired and Δt the point separation. After Fourier transformation, this leads to a pixel size of Δr given by Eqn. 9. The practical slice width is the smaller of the two. In practice, for GARField, that is usually Δr.

In ERICA, the pulse length was circa 2 μs, corresponding to a bandwidth of circa 500 kHz and a useful spatial field of view of about 1300 μm. The data sampling of 16 points at 1 MHz gives a spatial resolution of circa 160 μm and a pixel field of view of 2560 μm.

5.2. Data Analysis

In principle, the GARField echo train is treated in the same way as a CPMG echo train in bench top analyses, [1]. The decay is represented by

$$I(p\tau_{echo}) = \sum_{i=1}^{\epsilon} I_0^i \exp\left(\frac{-p\tau_{echo}}{T_2^i}\right) \qquad (19)$$

where $\tau_{echo} = 2\tau$. This works adequately but it should be recognised that, in the limit of very short τ, the quadrature sequence measures the spin lattice relaxation time in the rotating reference frame, $T_{1\rho}$ rather than T_2. The three relaxation times, T_2, T_1 and $T_{1\rho}$ are closely related but a full explanation is beyond the scope of this review.

As with SPRITE, some care is needed for accurate results.

- Echo intensity modulation

It is well known that the first few echoes of the quadrature sequence are modulated by weighting factors $w = \{w_1, w_2, w_3...\}$. The factors w_i oscillate about 1, but rapidly converge to 1 for $i \geq 2$. The effect arises because the pulse bandwidth expressed in frequency units

is very much less than the magnetic field dispersion due to the gradient, g spanning the sample length L also expressed in frequency units:

$$\frac{1}{t_p} \ll \frac{\gamma g L}{2\pi} \tag{20}$$

If the P^{90} pulse flip angle is accurately set at the slice centre, the excitation field is uniform over the sample and the sample is uniform along its length, then the weights can be calculated [19, 20]. For the quadrature echo sequence in particular they are $w = \left\{\frac{2}{3}, 1, 1, \frac{11}{12}, \cdots\right\}$. That the first echo intensity is ~66 % smaller than normal can usually be seen by eye and a correction made. However the assumptions underpinning the calculation are rarely met in practice and systematic errors can be introduced if intensities are simply multiplied by w. For this reason, we prefer to normalise all echo intensities using the signal intensity actually recorded from a spatially uniform, homogeneous rubber test sample. The assumption is made that the T_2 of the rubber is very long compared to the cement sample so that rubber signal relaxation can be ignored. If not, then the rubber T_2 relaxation must be accounted on the assumption that it is a unimodal exponential process. The rubber T_2 is measured ignoring the (modulated) early echoes. Finally, it is noted that a liquid sample cannot be used for the standard since the T_2 of liquids is very seriously shortened by molecular diffusion in the magnetic field gradient.

- Sensitive slice

The echo encompasses signal from across a region of sample of finite width dictated by the magnetic field gradient strength and pulse length. In order to select the signal originating only from the chosen depth, every echo was sine-bell filtered and Fourier transformed with respect to acquisition time relative to the echo centre. The absolute value of the signal intensity at the centre of the transformed spectrum was recorded as a measure of the signal from the selected depth.

The spectrometer and excitation pulse bandwidths attenuate the signal in the wings of the Fourier transformed spectrum (profile). Notwithstanding, intensity in the wings is sufficient to recognise the sample surface and to check for accurate sample positioning and levelling.

- Magnitude mode data

In ERICA, we recorded the magnitude mode Fourier transformed signal intensity. As with SPRITE, this leads to problems with baseline offset for low amplitude, slowly decaying components. However, and again like SPRITE, this was considered a more minor problem compared to phasing GARField data.

- Portlandite, ettringite *etc*

The necessarily short echo time required to well resolve hydrate inter-layer water led to some of the crystalline solid ($Ca(OH)_2$, ettringite *etc.*) signal coming through into the echo train decay. This was subtracted out as follows. In order to measure the "solid" contribution, a regular homogeneous magnetic field bench top experiment was carried out on equivalent cement samples before the experiment using the more common single quadrature echo sequence. The two pulses and echo of this sequence are identical to the start of the multiple quadrature echo sequence used in this work with GARField. The single echo sequence with variable τ_{echo} is used to differentiate evaporable and "solid" water. Hence the solid fraction in the first echo of the GARField experiment is found. Oven dried, analytical grade, $Ca(OH)_2$ was also measured in the homogeneous magnet using the multiple echo sequence with $\tau_{echo} = 40$ μs to get the best estimate possible for the decay curve for the "solid" in GARField. Then, thereby knowing the "solid" signal fraction in the first echo and the solid decay shape, the contribution due to crystalline solid was subtracted from all the GARField echo trains recorded. The key assumptions are that decay of $Ca(OH)_2$ is sufficiently representative of all the "solid" in the cement and that the amount of "solid" is independent of the degree of water saturation. It was checked experimentally that the shape of the decay curve in the homogeneous field was the same as in GARField. The former was used simply because it had a far superior signal-to-noise ratio.

- T_2 fitting

The remaining echo train intensity data was fit to a multi- exponential decay curve, Eqn. 19. Although good, the data was of insufficient signal-to-noise ratio to enable T_2 fitting by inverse Laplace transformation. Rather, on the basis of previously published work, the decays were fit to a 3 component exponential decay with constrained T_2 decay times using a least squares algorithm. The T_2 values were chosen by careful analysis of hydrated samples and by comparison with earlier work using homogeneous magnetic field NMR on similar cements. The T_2 values were considered constants throughout the experiments. This methodology ignores gradual changes resultant from gradual changes in average pore size for any given pore type and any change in

distribution within that type but does satisfactorily assign values to the three (water filled) pore size fractions. It also ignores minor differences between true T_2 decay and the T_2 - $T_{1\rho}$ amalgam that is manifest with the multi-echo quadrature sequence sequence.

Experimental results obtained using GARField applied to cement within ERICA are to be found in the literature, [21].

6. Unilateral magnets

Unilateral magnets for sub-surface NMR have a long history [23]. They are especially developed within the petroleum industry for imaging at depth within large rocks including down bore-hole [25, 26] although they have also been used for exploratory work on cement systems [27, 28]. A useful review is to be found within the wider review of ^{1}H NMR applied to construction materials by Nagel *et. al* [24]. Most of these cement studies have used a variation of the so-called NMR-MOUSE [23] limiting sample size, or at least depth of penetration, to a few millimetres. In an earlier EC MSCA project, TRANSCEND, we used a unilateral GARField design [29, 28] to select and measure a slice of concrete at a depth of a few centimetres in a block measuring circa 15 by 15 by 10 cm^3 Although useful results were obtained concerning porosity relaxation in response to sorption [30] and depth of water penetration compared to colour change [31], a practical difficulty was that the gradient strength was too strong and so the selected slice too narrow and so the signal-to-noise ratio per scan too low, in order to make overall data acquisition times sufficiently short for routine application. Hence, within ERICA, a new magnet was designed to a very different gradient specification. This magnet was built using the barrel magnet concept proposed by Fukushima and Jackson [22], and further developed by Utsuzawa and Fukushima [32].

The design comprises an annular barrel magnet with a cylindrical magnet positioned on-axis, inside, just below the surface Fig. 7a. By careful selection of the relative magnet sizes and strength and on-axis position, it is possible to arrange for a region of near uniform magnetic field offset from the end of the device by a few centimetres. Fig. 7c shows the magnet used in ERICA under construction. The barrel is made from three layers of 4 concentric rings of permanent magnets each 2.5 cm^3. The cylinder is two layers of 3 rings including the centre magnet. A total of 440 magnets are used. The overall magnet including housing measures about 50 cm in diameter and 11 cm in depth.

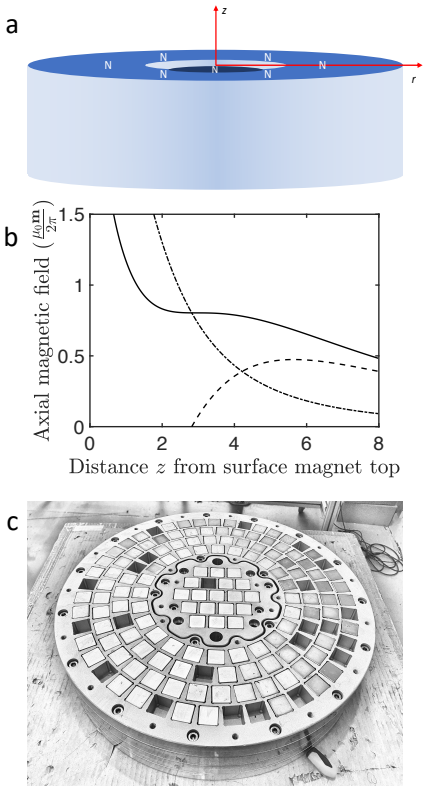

Figure 7: (a). A schematic of a barrel magnet [22]. (c) The barrel magnet as used in ERICA under construction at MR Solutions. It is built from 440 2.5 cm^3 permanent magnets as described in the text and is about 50 cm in diameter. (b) The solid line is the on-axis field strength calculated assuming each magnet is a point dipole (**m**) and that they are arranged uniformly in concentric circles and layers as described in the text. The distance unit corresponds to one magnet block spacing, centre to-centre, along z. The field profile corresponds well to the finite element modelling design specification and measurement of the actual magnetic field. The dot-dash and dash lines are the contributions from the cylinder and barrel respectively.

Although the actual design was optimised using finite element modelling software, a good approximation to the field profile along the axis is quickly obtained by treating each magnet cube as a point dipole **m** appropriately spaced on a cylindrical polar co-ordinate lattice with equal radial and longitudinal unit spacing. The radii used are $\{0, 1, 2, 4, 5, 6, 7\}$ and the magnets per ring are $\{1, 6, 12, 24, 30, 37, 43\}$. With an offset between the barrel (radii= $\{0, 1, 2\}$) and cylinder (radii=$\{4, 5, 6, 7\}$) magnets of -0.64 lattice units, the design creates a "sweet-spot" of notionally uniform field above the barrel surface as shown in Fig. 7b. The position and uniformity of the sweet-spot can be adjusted a little by moving the cylinder magnet longitudinally with respect to the barrel.

	SPRITE	GARField	Unilateral magnet
Magnet	1.5 T, 20 cm bore super-conducting	GARField design, permanent, see ref. [17]	Barrel design, permanent, see ref. [22]
NMR frequency (MHz)	60	30	2
Sample size (mm) & shape	60; cylinder	1; disc	≥150; cube
Resolution (mm)	1 - 2	0.1 - 0.2	5 - 10
Localisation	Spatial profile	Spot measurement at selected depth	Spot measurement at selected depth
Typical measurement time (temporal resolution, minutes)	13	4	20
Typical pulse sequence	SPRITE	Quadrature echo train	CPMG
Typical pulse length (μs)	10-20	2-5	40-70
Dead time (μs)	10-20	5-10	80-100
Capillary water	✓	✓	✓
Gel water	✓	✓	✓
Inter-layer water	unreliable	✓	semi-qauntitative
Solids	✗	independent measurement, calibrate & subtract	✗

Table 1: A comparative table for SPRITE, and GARField and large Unilateral Magnet analysis of cements and concretes as experienced within ERICA. Smaller unilateral magnets, such as a small NMR MOUSE [23, 24], may perform closer to GARField but were not used within ERICA.

The magnet as built within ERICA was fitted with a planar radio frequency excitation coil in a "square-spiral", figure-of-8 design. It was designed to measure signal from a slice a few millimetres thick situated ~ 30 mm below the surface of a block of cement, mortar or concrete typically $15 \times 15 \times 15$ cm^3 or larger in size, using either a CPMG,

$$P_x^{90} - \tau - \left(P_y^{180} - 2\tau -\right)_n$$

or multi-quadrature echo,

$$P_x^{90} - \tau - \left(P_y^{90} - 2\tau -\right)_n$$

pulse sequence. As with GARField, due to the limited pulse bandwidth compared to the magnet inhomogeneity, Eqn. 20, there is considerable echo modulation. It is treated in the same way: by measuring, and normalising to, the signal from a uniform standard sample.

6.1. Exemplar results

Fig. 8 shows exemplar results recorded from a mortar sample measuring $20 \times 15 \times 6$ cm^3 using a CPMG sequence. Signal is recorded from 3 cm deep in the block, *i.e.* the mid-plane. The NMR frequency was 1.9 MHz. At these low frequencies, and with long excitation pulse lengths of typically 60 μs the spectrometer dead-time is about 90 μs. Hence, the first echo that can be reliably measured is at an echo time $2\tau = 280$ μs. 1200 scans were recorded for averaging with a recycle delay of 1 s.

Fig 8a and b show echo train intensities measured immediately after mixing and 24 hours after mixing respectively. They each took 20 minutes to acquire, although, in reality there was good signal-to-noise after 2 - 3 minutes. Notice how the first echoes in particular are attenuated by a factor of about $\frac{2}{3}$ due to the magnetic field inhomogeneity spanning the sample, expressed as a frequency bandwidth, exceeding that of the excitation pulses, as previously discussed. Fig. 8c and d show the echo intensities of the same trains after normalisation by a standard rubber sample to correct for this modulation. A 4 component exponential decay fit with constrained relaxation time values of $\{400, 1600, 6400, 25600\}$ μs are also shown. The fit intensities as a function of hydration time are shown in Fig. 8e: one data point every 20 minutes for 1 week. Hydrate densification over that time is very clear. The relaxation time of the dominant relaxation component gets progressively shorter and the total evaporable water signal intensity gets smaller.

It might have been thought that the long first echo time would totally preclude observation of hydrate

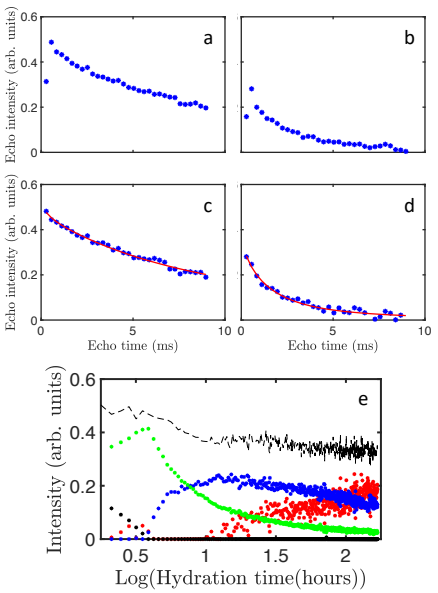

Figure 8: Echo trains recorded 3 cm below the surface of a block of mortar (a) immediately after mixing and (b) after 24 hours hydration using a unilateral magnet. (c) and (d) are the echo trains (a) and (b) respectively corrected by a standard sample for early echo modulation. (e) Relaxation component fit intensities as a function of hydration time: for relaxation times of 0.4 (red), 1.6 (blue), 6.4 (green) and 25.6 (black) ms. The mirror symmetry in the black and green traces in the early hours of hydration is likely an artefact of fitting a gradually decreasing, but broad, relaxation time population to two discrete values. The dash line is the total intensity and represents (nearly all, see text) evaporable water.

inter-layer water and make observation of gel water difficult. The data and our ERICA experience is rather different. First notice that the overall intensity sum reduces by about 30 % over the course of the hydration. This is more than would be expected if the loss were due entirely to the creation of quasi-crystalline phases with extremely short relaxation times ($\sim$ 10 μs) such as Portlandite, that normally consume about 20-25 % of the mix water. However, it is not enough to include all of the hydrate inter-layer water ($T_2 \sim 100-150$ μs) as well as the quasi-crystalline phases, that together consume $\approx$ 60 % [33, 34]. This suggests that most evaporable water, including a significant quantity of the hydrate inter-layer water, is seen in this experiment. We therefore conclude that the shortest relaxation time component (400 μs) represents most of the inter-layer water. This means that the next component (1600 μs) must be predominantly gel water. The longest two relaxation time components would then cover inter-hydrate and capillary water together. Such relaxation times are considerably longer than those observed for T_2 in regular bench top measurements or in the SPRITE or GARField experiments discussed above. We believe that in the open-access experiment the mark to space (or on-time to off-time) ratio of the excitation pulses is sufficiently large that we are measuring a relaxation time more akin to $T_{1\rho}$ than T_2. Here the mark-space ratio is about 0.2. With our bench top, GARField and SPRITE implementations the ratios are $\lesssim \{0.08, 0.06, 0.03\}$ respectively. Alternatively, there is a large frequency dependence in the relaxation time. The unilateral magnet experiment is at 1.9 MHz. Our bench-top, GARField and SPRITE operate at $\{20, 30, 60\}$ MHz respectively. However, we consider this less likely to be the cause than $T_{1\rho}$ given the known frequency dependencies as reported in, for instance, [35]. If this preliminary analysis is right, then we conclude that it is easily possible to measure gel water in mortar as well as some residual inter-layer water in the first few echoes.

7. Comparison of Methodology

In conclusion, Table 1 seeks to compare the different methods of obtaining spatially localised ^{1}H NMR information from cement based materials as implemented within ERICA.

Acknowledgements

This work has received funding from the European Union Horizon 2020 Research and Innovation Programme under the Marie Skłodowska-Curie Innovative Training Networks programme grant agreement No. 764691.

References

[1] P. J. McDonald, A. M. Gajewicz-Jaromin, R. Morrell, The characterisation of cement based materials using T2 1H nuclear magnetic resonance relaxation analysis., NPL Good Practice Guide 144 (2017) 1–165. ISSN 1368–6550.

[2] A. J. Bohris, U. Goerke, P. J. McDonald, M. Mulheron, B. Newling, B. Le Page, A broad line NMR and MRI study of water and water transport in portland cement pastes, Magn. Reson. Imag. 16 (1998) 455–461.

[3] S. Zamani, R. M. Kowalczyk, P. J. McDonald, The relative humidity dependence of the permeability of cement paste measured using GARField NMR profiling, Cem. Conc. Res. 57 (2014) 88–94.

[4] S. D. Beyea, B. J. Balcom, T. W. Bremner, P. J. Prado, D. P. Green, R. L. Armstrong, P. E. Grattan-Bellew, Magnetic resonance imaging and moisture content profiles of drying concrete, Cem. Conc. Res. 28 (1998) 453–463.

[5] L. Pel, K. Hazrati, K. Kopinga, J. Marchand, Water absorption in mortar determined by NMR, Magn. Reson. Imag. 16 (1998) 525–528.

[6] A. Leventis, D. A. Verganelakis, M. R. Halse, J. B. W. Webber, J. H. Strange, Capillary Imbibition and Pore Characterisation in Cement Pastes, Transp Porous Med 39 (2000) 143–157.
[7] P. F. Faure, S. Caré, J. Magat, T. Chaussadent, Drying effect on cement paste porosity at early age observed by NMR methods, Construction and Building Materials 29 (2012) 496–503.
[8] M. Van Landeghem, J.-B. d'Espinose de Lacaillerie, B. Blümich, J. P. Korb, B. Bresson, The roles of hydration and evaporation during the drying of a cement paste by localized NMR, Cem. Conc. Res. 48 (2013) 86–96.
[9] R. Enjilela, P. F. de J Cano-Barrita, A. Komar, A. J. Boyd, B. J. Balcom, Wet front penetration with unsteady state wicking in mortar studied by Magnetic Resonance Imaging (MRI), Mater. Struct. 51 (2018) 1–16.
[10] W. A. Edelstein, J. M. S. Hutchison, G. Johnson, T. Redpath, Spin warp NMR imaging and applications to human whole-body imaging, Physics in Medicine and Biology 25 (1980) 751–756.
[11] S. D. Beyea, B. J. Balcom, P. J. Prado, A. R. Cross, C. B. Kennedy, R. L. Armstrong, T. W. Bremner, Relaxation Time Mapping of Short T2* Nuclei with Single-Point Imaging (SPI) Methods, J. Magn. Reson. 135 (1998) 156–164.
[12] L. Li, H. Han, B. J. Balcom, Spin echo SPI methods for quantitative analysis of fluids in porous media, J. Magn. Reson. 198 (2009) 252–260.
[13] B. J. Balcom, SPRITE imaging of short relaxation time nuclei, in: P. Blmler, B. Blmich, R. Botto, E. Fukushima (Eds.), Spatially Resolved Magnetic Resonance, Wiley-VCH Verlag GmbH, Weinheim, Germany, 1998, pp. 75–86.
[14] H. Y. Carr, Steady-State Free Precession in Nuclear Magnetic Resonance, Phys. Rev. 112 (1958) 1693.
[15] W. S. Hinshaw, Image formation by nuclear magnetic resonance: The sensitive-point method, J. Appl. Phys. 47 (2008) 3709.
[16] M. Janota, O. Istok, D. A. Faux, P. J. McDonald, Factors influencing the time dependence of porosity relaxation in cement during sorption: Experimental results from spatially resolved nmr., Submitted to Cement (2021).
[17] P. M. Glover, P. S. Aptaker, J. R. Bowler, E. Ciampi, P. J. McDonald, A Novel High-Gradient Permanent Magnet for the Profiling of Planar Films and Coatings, J. Magn. Reson. 139 (1999) 90–97.
[18] P. J. McDonald, B. Newling, Stray field magnetic resonance imaging, Reports on Progress in Physics 61 (1998) 1441–1493.
[19] T. B. Benson, P. J. McDonald, Profile Amplitude Modulation in Stray-Field Magnetic-Resonance Imaging, J. Magn. Reson. A 112 (1995) 17–23.
[20] M. D. Hurlimann, D. D. Griffin, Spin Dynamics of Carr–Purcell–Meiboom–Gill-like Sequences in Grossly Inhomogeneous B0 and B1 Fields and Application to NMR Well Logging, J. Magn. Reson. 143 (2000) 120–135.
[21] P. J. McDonald, O. Istok, M. Janota, A. M. Gajewicz-Jaromin, D. A. Faux, Sorption, anomalous water transport and dynamic porosity in cement paste: A spatially localised 1H NMR relaxation study and a proposed mechanism, Cem. Conc. Res. 133 (2020) 106045.
[22] E. Fukushima, J. A. Jackson, Unilateral magnet having a remote uniform field region for nuclear magnetic resonance, US Patent 6828892B1 (2002).
[23] G. Eidmann, R. Savelsberg, P. Blümler, B. Blümich, The NMR MOUSE, a Mobile Universal Surface Explorer , J. Magn. Reson. A 122 (1996) 104–109.
[24] S. M. Nagel, C. Strangfeld, S. Kruschwitzwitz, Application of 1H Proton NMR Relaxometry to Building Materials-A Review, J. Magn. Reson. Open 6-7 (2021) 100012.
[25] R. L. Kleinberg, J. A. Jackson, An introduction to the history of NMR well logging, Conc. MAgn. Reson. 13 (2001) 340–341.
[26] R. de Oliveira-Silva, É. Lucas-Oliveira, A. G. de Araújo-Ferreira, W. A. Trevizan, E. L. G. Vidoto, D. Sakellariou, T. J. Bonagamba, A benchtop single-sided magnet with NMR well-logging tool specifications - Examples of application., J. Magn. Reson. 322 (2021) 106871.
[27] P. F. de J Cano-Barrita, B. J. Balcom, F. Castellanos, Carbonation front in cement paste detected by T 2 NMR measurements using a low field unilateral magnet, Materials and Structures 50 (2017) 150 (1–8).
[28] P. F. de J Cano-Barrita, F. Díaz-Díaz, Moisture Distribution during Water Absorption of Ordinary Portland Cement Mortars Obtained with Low-Field Unilateral Magnetic Resonance, Materials 14 (2021) 4279 (1–15).
[29] P. J. McDonald, P. S. Aptaker, J. Mitchell, M. Mulheron, A unilateral NMR magnet for sub-structure analysis in the built environment: The Surface GARField, J. Magn. Reson. 185 (2007) 1–11.
[30] N. Fischer, R. Haerdtl, P. J. McDonald, Observation of the redistribution of nanoscale water filled porosity in cement based materials during wetting, Cem. Conc. Res. 68 (2015) 148–155.
[31] N. Fischer, P. J. McDonald, R. Haerdtl, Is colour change a good measure of a water penetration front?, Magazine of concrete research 67 (2015) 1048–1053.
[32] S. Utsuzawa, E. Fukushima, Unilateral NMR with a barrel magnet., J. Magn. Reson. 282 (2017) 104–113.
[33] A. C. A. Muller, K. L. Scrivener, A. M. Gajewicz, P. J. McDonald, Densification of C–S–H Measured by 1H NMR Relaxometry, J. Phys. Chem. C 117 (2013) 403–412.
[34] A. C. A. Muller, K. L. Scrivener, A. M. Gajewicz, P. J. McDonald, Use of bench-top NMR to measure the density, composition and desorption isotherm of CSH in cement paste, Microporous and Mesoporous Materials 178 (2013) 99–103.
[35] F. Barberon, J. P. Korb, D. Petit, V. Morin, E. Bermejo, Probing the Surface Area of a Cement-Based Material by Nuclear Magnetic Relaxation Dispersion, Phys. Rev. Lett. 90 (2003) 116103.